Neutron star radius measurement from the ultraviolet and soft X-ray thermal emission of PSR J0437–4715

Denis Gonzalez-Caniulef, Sebastien Guillot, Andreas Reisenegger

Monthly Notices
of the
ROYAL ASTRONOMICAL SOCIETY

MNRAS **490,** 5848–5859 (2019) doi:10.1093/mnras/stz2941

Neutron star radius measurement from the ultraviolet and soft X-ray thermal emission of PSR J0437−4715

Denis González-Caniulef,[1,2]★ Sebastien Guillot [3,4] and Andreas Reisenegger[2]

[1]*Mullard Space Science Laboratory, University College London, Holmbury St Mary, Dorking, Surrey RH5 6NT, UK*
[2]*Instituto de Astrofísica, Facultad de Física, Pontificia Universidad Católica de Chile, Av. Vicuña Mackenna 4860, 8970436 Macul, Santiago, Chile*
[3]*IRAP, CNRS, 9 avenue du Colonel Roche, BP 44346, F-31028 Toulouse Cedex 4, France*
[4]*Université de Toulouse, CNES, UPS-OMP, F-31028 Toulouse, France*

Accepted 2019 October 11. Received 2019 October 11; in original form 2019 April 30

ABSTRACT

We analysed the thermal emission from the entire surface of the millisecond pulsar PSR J0437−4715 observed in the ultraviolet and soft X-ray bands. For this, we calculated non-magnetized, partially ionized atmosphere models of hydrogen, helium, and iron compositions and included plasma frequency effects that may affect the emergent spectrum. This is particularly true for the coldest atmospheres composed of iron (up to a few per cent changes in the soft X-ray flux). Employing a Markov chain Monte Carlo method, we found that the spectral fits favour a hydrogen atmosphere, disfavour a helium composition, and rule out iron atmosphere and blackbody models. By using a Gaussian prior on the dust extinction, based on the latest 3D map of Galactic dust, and accounting for the presence of hot polar caps found in the previous work, we found that the hydrogen atmosphere model results in a well-constrained neutron star radius $R_{\rm NS} = 13.6^{+0.9}_{-0.8}$ km and bulk surface temperature $T_{\rm eff}^{\infty} = (2.3 \pm 0.1) \times 10^5$ K. This relatively large radius favours a stiff equation of state and disfavours a strange quark composition inside neutron stars.

Key words: dense matter – equation of state – plasmas – stars: atmospheres – stars: neutron – pulsars: individual (PSR J0437−4715).

1 INTRODUCTION

The study of the thermal emission from neutron stars (NSs) is particularly relevant to understand their cooling history, determine their radii, and constrain the equation of state (EOS) of ultradense matter. In general, the thermal emission from NSs is expected to be reprocessed by an atmosphere, whose spectrum depends on the temperature gradient, surface composition, and magnetic field strength of the source. There already exists substantial literature dedicated to the effects of these parameters on the emergent spectra of relatively hot NS atmospheres, with temperature $T > 10^6$ K (for reviews, see e.g. Zavlin 2007; Özel 2013; Potekhin 2014).

The spectra of cooler NS atmospheres, in which plasma effects start to become important, have been less studied. However, these atmosphere models are relevant for analysing the thermal emission from old NSs (ages $> 10^6$ yr), such as millisecond pulsars (MSPs), which have lost most of their thermal energy. Up to now, *Hubble Space Telescope* (*HST*) observations have revealed ultraviolet (UV) emission from two MSPs, PSR J0437−4715 (hereafter 'J0437'; Kargaltsev, Pavlov & Romani 2004; Durant et al. 2012) and PSR J2124−3358 ('J2124'; Rangelov et al. 2017), and from the middle-aged classical pulsar PSR B0950+08 ('B0950'; Pavlov et al. 2017). In all three cases, the interpretation of the thermal spectrum as blackbody (BB) emission yields bulk surface temperatures of around 10^5 K, whereas an upper limit of 4×10^4 K was inferred from the non-detection of the old, very slow pulsar PSR J2144−3933 (Guillot et al. 2019). More realistic estimates of the surface temperature of these objects, using atmosphere models, will help to distinguish between different possible heating mechanisms in old NSs (Gonzalez & Reisenegger 2010). This would in turn provide constraints on NS internal parameters, such as the superfluid energy gaps, which regulate the strength of these mechanisms (Petrovich & Reisenegger 2010, 2011; González-Jiménez, Petrovich & Reisenegger 2015).

Furthermore, J0437 and J2124, as well as PSR J0030+0451 ('J0030'), are among the targets of the *Neutron Star Interior Composition Explorer* mission (*NICER*; Gendreau et al. 2016; Gendreau & Arzoumanian 2017). *NICER* aims at measuring the mass $M_{\rm NS}$ and radius $R_{\rm NS}$ of these MSPs through the effect of gravitational light bending and other relativistic effects on their X-ray light curves produced by hot polar caps (Bogdanov 2013; Miller 2016; Özel et al. 2016). In fact, combined analysis of hydrogen atmosphere models with *XMM–Newton* X-ray spectral/timing observations of the hot polar cap emission has permitted establishing some constraints on the radii of J2124, J0030, and J0437, which, assuming an NS mass

★ E-mail: denis.caniulef.14@ucl.ac.uk

$M_{\rm NS} = 1.4\,{\rm M}_{\odot}$, resulted in $R_{\rm NS} > 7.8$ km (68 per cent confidence; Bogdanov, Grindlay & Rybicki 2008), $R_{\rm NS} > 10.4$ km (99 per cent confidence; Bogdanov & Grindlay 2009), and $R_{\rm NS} > 10.9$ km (3σ confidence; Bogdanov 2013), respectively. In light of upcoming *NICER* analyses, it is therefore important to characterize the atmospheric properties of MSPs (e.g. composition and temperature) as accurately as possible to establish further constraints on the properties of these sources.

We model non-magnetized, partially ionized NS atmospheres for temperatures down to $\sim 10^{4.5}$ K, and fit them to the UV and soft X-ray spectra of J0437. Besides being the main target for *NICER*, J0437 is the brightest and nearest MSP, with a precisely measured distance $d = 156.79 \pm 0.25$ pc (Reardon et al. 2016). In addition, it is in a 5.74 d binary orbit with a helium-core white dwarf companion (Bailyn 1993), allowing for a precise radio-timing measurement of the pulsar mass, $M_{\rm NS} = 1.44 \pm 0.07\,{\rm M}_{\odot}$ (Reardon et al. 2016). The white dwarf has an effective temperature of 3950 ± 150 K (Durant et al. 2012), making it very unlikely to contribute significantly to the UV emission of the system. The spin period of J0437, $P = 5.76$ ms, and its spin-down rate, $\dot{P} = 5.73 \times 10^{-20}\,{\rm s\,s^{-1}}$, imply a large spin-down age (after kinematic corrections), $\tau = P/2\dot{P} = 6.7$ Gyr, and a weak dipole magnetic field, $B = 2.8 \times 10^8$ G.

The X-ray spectrum of J0437 is composed of two thermal components from the pulsar's hot polar caps (Zavlin & Pavlov 1998), generally fitted with a pair of NS atmosphere components (with $T \sim 10^6$ K), and a non-thermal component fitted with a power law (Zavlin et al. 2002). Because of its proximity, J0437 is also the only MSP for which the $\sim 10^5$ K thermal emission from the entire pulsar surface is detectable in the soft X-ray range below ~ 0.4 keV. This third (cool) thermal component is clearly seen in the UV (Kargaltsev et al. 2004; Durant et al. 2012), but it was poorly constrained in studies that only considered the X-ray data, due to uncertain contributions of a non-thermal component (Bogdanov 2013). This is so because the mild excess below ~ 0.4 keV in the *XMM* data could be compensated by a soft power law. More recent work used *NuSTAR* observations to better constrain the high-energy tail (at $\gtrsim 4$ keV), which lifted ambiguities with the spectral modelling at lower energies ($\lesssim 0.4$ keV). Combined *ROSAT*, *XMM–Newton*, and *NuSTAR* spectral analysis confirmed the presence of this third thermal component (with $T \sim 10^5$ K, fitted with a BB), which was interpreted as the thermal emission coming from the entire surface (Guillot et al. 2016).

However, only the Wien tail of this cool surface emission is detected in the soft X-ray regime. Therefore, its minimal contribution to the X-ray flux in the 0.1–0.5 keV range, affected by absorption due to the interstellar medium, and dominated by the hotter thermal components, prevented precisely determining the surface temperature and emitting area (i.e. the NS radius). In addition to the evidence for the cool thermal emission in the soft X-rays, J0437 is also the only pulsar for which one can precisely determine, thanks to the pulsar's proximity, the slope of this emission in the UV band with spectroscopic observations (Kargaltsev et al. 2004; Durant et al. 2012).

This paper aims at obtaining better constraints on the cool thermal emission of J0437 by combining the UV and soft X-ray observations. We model and apply realistic NS atmosphere models, for various compositions, to the UV data from *HST* and soft X-ray data from *ROSAT*. The organization of the article is as follows. In Section 2, we describe the theoretical framework to compute the emergent spectrum from an NS atmosphere, and how we introduce the plasma effects. In Section 3, we verify the accuracy of our models and investigate their properties, particularly the plasma effects. In Section 4, we confront our atmosphere models for different compositions to the observed UV to soft X-ray spectral energy distribution of J0437. A summary of our main conclusions and the discussion are given in Section 5.

2 THEORETICAL FRAMEWORK

Substantial literature on both magnetic and non-magnetic NS atmosphere models already exists (for reviews, see Zavlin 2007; Özel 2013; Potekhin 2014). In particular, spectra from non-magnetized, passively cooling NSs are usually obtained via the computation of the atmosphere structure coupled with (i) the Milne integral (Romani 1987; Rajagopal & Romani 1996; Pons et al. 2002), (ii) the radiative transfer equation in the form of a second-order boundary problem (Zavlin, Pavlov & Shibanov 1996; Heinke et al. 2006; Suleimanov & Werner 2007; Haakonsen et al. 2012), or (iii) the radiative transfer equation using the Rybicki method (Gänsicke, Braje & Romani 2002).

2.1 Neglect of magnetic effects

The criteria to establish whether non-magnetized atmospheres are suitable for analyses of the thermal emission from different classes of NSs consider the temperature, spectral energy range, and magnetic field strength of the source. Basically, a magnetic field changes the properties of the atmosphere in two ways: by modifying the energy levels of the atoms, which changes the bound–bound and bound–free opacities, and by modifying the dynamics of free electrons with kinetic energy below the electron cyclotron energy, which changes the free–free opacities. Considering the electron cyclotron energy $E_{\rm c} = \hbar e B/m_{\rm e}c \approx 1\,B_8$ eV, magnetic fields are negligible for the bound–bound and bound–free opacities if the ratio $E_{\rm c}/Z^2{\rm Ry} \sim 0.1\,B_8\,Z^{-2} \ll 1$, where Z is the atomic number, ${\rm Ry} = 13.6$ eV is the Rydberg energy, and $B_8 = B/10^8$ G. Similarly, for the free–free opacities, magnetic fields are negligible if the ratio $E_{\rm c}/k_{\rm B}T \sim 0.1\,B_8/T_5 \ll 1$, with $T_5 = T/10^5$ K, or the spectral energy range of interest is above the electron cyclotron energy, $E \gg E_{\rm c} \approx 1\,B_8$ eV.

Spectra for *fully ionized* atmosphere models of NSs with different field strengths have been reported, for example, in fig. 2.7 of Lloyd (2003). In particular, for the lowest temperature considered in that work, $\log(T/{\rm K}) = 5.6$, the spectrum for $B = 10^8$ G is indistinguishable from that of a non-magnetic NS. As also shown in the same figure, the magnetic field produces an absorption feature around the electron cyclotron energy. In the case of J0437, the magnetic field is $B_8 \approx 2.8$, the associated electron cyclotron frequency is $\log(E_{\rm c}/{\rm keV}) = -2.6$, and we will fit the spectrum to UV data well above this value, for $\log(E/{\rm keV}) > -2.2$, finding typical temperatures $T_5 \sim 3$.

Depending on the composition, *partially ionized* atmospheres show absorption features at different energies. In particular, the H atmosphere spectrum has a Lyman alpha absorption feature at $E = 10.2$ eV, which, depending on the NS gravitational redshift, can be within the range of the UV *HST* observations. Magnetic fields such as those present in MSPs are strong enough to induce a large Zeeman effect, i.e. the splitting of the Lyman alpha absorption feature into three separate components (see e.g. Kargaltsev et al. 2004). These are expected to be washed out in the measured, phase-averaged spectrum, because the latter combines radiation from different parts of the NS surface, where the magnetic field strength and direction are expected to be very different, thus placing the absorption components at different wavelengths. Therefore, we

will ignore the presence of the magnetic field in our atmosphere model calculations. For the spectral fitting of J0437 (Section 4.2), we eliminate the Lyman alpha absorption feature from the spectra of the H atmosphere models by linearly interpolating through the spectral range covered by this feature.

Another important effect of magnetic fields on NS atmospheres is that they can suppress convective instabilities. As shown by Rajagopal & Romani (1996), a pure iron atmosphere with $T \sim 10^5$ K is unstable to convective motion in zones of the atmospheres with optical depths $\tau \sim 0.1$–1.0, which could modify the temperature gradient of the atmosphere and produce a dramatic effect in the emergent spectra. However, they also showed that a magnetic field $B \gtrsim 10^7$ G can suppress this instability and therefore it should not be present in the atmospheres of MSPs. Consistently, our models do not include convection.

2.2 Atmosphere model calculations

We use our own new code based on the iterative scheme discussed in Romani (1987) (see also Rajagopal & Romani 1996; Pons et al. 2002) to simultaneously calculate the atmosphere structure and the spectral energy distribution via the Milne integral, for the case of unmagnetized NSs with low temperatures. It imposes that the NS atmosphere is in hydrostatic and radiative equilibrium. The latter means that the radiative flux through the atmosphere is constant and there is no additional source of energy. Because the thickness of the atmosphere is much smaller than the radius of the star, the radiative transfer equation is solved in the plane-parallel approximation, assuming the atmosphere is in local thermodynamic equilibrium.

In order to determine the structure of the atmosphere, we solve the equation of hydrostatic equilibrium

$$\frac{\mathrm{d}P}{\mathrm{d}\tau_{\mathrm{R}}} = \frac{g_{\mathrm{eff}}}{\kappa_{\mathrm{R}}}, \tag{1}$$

where P is the pressure, κ_{R} is the Rosseland mean opacity (defined later in equation 9), and $\mathrm{d}\tau_{\mathrm{R}} = \rho\kappa_{\mathrm{R}}\,\mathrm{d}\ell$, with ρ and ℓ the density and physical depth of the atmosphere, respectively. Here, for a given mass M_{NS} and coordinate radius R_{NS}, the gravitational acceleration $g_{\mathrm{eff}} = (1+z)\,GM_{\mathrm{NS}}/R_{\mathrm{NS}}^2$ and the gravitational redshift $1+z = (1-2GM_{\mathrm{NS}}/R_{\mathrm{NS}}\,c^2)^{-1/2}$, where G and c correspond to the gravitational constant and the speed of light, respectively. For equation (1), we use the boundary condition $P(\tau_{\mathrm{R}}=0)=0$ and an ideal gas EOS, adding the pressure of degenerate electrons, which becomes relevant in the deepest zones of the atmosphere.

The problem is solved through successive iterations, starting from an initial temperature profile given by the solution for the grey atmosphere, $T^4 = (3/4)\,T_{\mathrm{eff}}^4(\tau_{\mathrm{R}}+q)$, where T_{eff} is the effective temperature and $q = 2/3$. Subsequently, we calculate the energy-dependent flux through the atmosphere. Since the absorptive opacity $\kappa_E^{\mathrm{a}} \sim 10^3$–$10^5\,\mathrm{cm^2\,g^{-1}}$ is much larger than the electron scattering opacity $\kappa^{\mathrm{sc}} \approx 0.1$–$0.2\,\mathrm{cm^2\,g^{-1}}$, we neglect the electron scattering effects. In this way, the expression for the energy-dependent flux reduces to the Milne integral (Mihalas 1978)

$$F_E(\tau_E) = 2\pi\left[\int_{\tau_E}^{\infty} S_E\left(\tau_E'\right) E_2\left(\tau_E'-\tau_E\right)\mathrm{d}\tau_E' - \int_0^{\tau_E} S_E\left(\tau_E'\right) E_2\left(\tau_E-\tau_E'\right)\mathrm{d}\tau_E'\right], \tag{2}$$

where the source function $S_E(x)$ is just the Planck function,

$$E_2(x) = \int_1^{\infty} \frac{\mathrm{e}^{-xt}}{t^2}\mathrm{d}t \tag{3}$$

is the second exponential integral, and

$$\tau_E = \int_0^{\tau_{\mathrm{R}}} \frac{\kappa_E}{\kappa_{\mathrm{R}}}\mathrm{d}\tau_{\mathrm{R}}' \tag{4}$$

gives the transformation from Rosseland mean to energy-dependent optical depths.

Finally, in order to obtain a specified, constant energy-integrated radiative flux through the atmosphere, $F = \sigma T_{\mathrm{eff}}^4$, we apply the Lucy–Unsöld correction to the temperature profile, which is given by

$$\Delta T(\tau) = \frac{1}{16\sigma T(\tau)^3}\left[\frac{\kappa_J}{\kappa_{\mathrm{P}}}\left(3\int_0^{\tau}\frac{\kappa_F\left(\tau'\right)}{\kappa_{\mathrm{R}}\left(\tau'\right)}\Delta F\left(\tau'\right)\mathrm{d}\tau' + 2\Delta F(0)\right) - \frac{\kappa_{\mathrm{R}}}{\kappa_{\mathrm{P}}}\frac{\mathrm{d}\Delta F(\tau)}{\mathrm{d}\tau_{\mathrm{R}}}\right], \tag{5}$$

where ΔF is the departure from the specified, constant flux F. In the previous expression, the quantities

$$\kappa_J \equiv \int_0^{\infty} \kappa_E^{\mathrm{a}} J_E\,\mathrm{d}E\big/J, \tag{6}$$

$$\kappa_{\mathrm{P}} \equiv \int_0^{\infty} \kappa_E^{\mathrm{a}} B_E\,\mathrm{d}E\big/B, \tag{7}$$

$$\kappa_F \equiv \int_0^{\infty} (\kappa_E^{\mathrm{a}}+\kappa^{\mathrm{sc}}) F_E\,\mathrm{d}E\big/F, \tag{8}$$

and

$$\frac{1}{\kappa_{\mathrm{R}}} \equiv \int_0^{\infty} \frac{1}{\kappa_E^{\mathrm{a}}+\kappa^{\mathrm{sc}}}\frac{\mathrm{d}B_E}{\mathrm{d}T}\mathrm{d}E\Big/\frac{\mathrm{d}B}{\mathrm{d}T} \tag{9}$$

are the absorption mean, Planck mean, flux mean, and Rosseland mean opacities, respectively (Mihalas 1978). Here, J and B are the mean intensity and Planck function integrated in energy, respectively, and we approximate $\kappa_J = \kappa_{\mathrm{P}}$. A relatively constant flux (error $\lesssim$1 per cent) is reached in ∼15 iterations. In this procedure, we take into account the corrections from general relativity in the emergent spectrum. This means that the flux measured by an observer at distance D is

$$F_E^{\infty}(E) = \frac{F_E([1+z]\,E)}{1+z}\left(\frac{R_{\mathrm{NS}}}{D}\right)^2, \tag{10}$$

where $F_E([1+z]E)$ is the flux at the NS surface.

In order to compute the emergent spectrum, we use 100 energy bins logarithmically spaced from 10^{-4} to 10 keV and a grid of 120 depth levels logarithmically spaced in Rosseland optical depth, τ_{R}, from 10^{-3} to 10^3. Once the proper atmosphere structure is iteratively obtained, the spectrum is calculated using a denser grid with 900 energy bins. We use the energy-dependent opacities and the Rosseland and Planck mean opacities for H, He, and Fe from the Los Alamos Opacity Project[1] (LANL; Magee et al. 1995), which include bound–bound, bound–free, and free–free transitions. The LANL opacity tables also provide the number of free electrons per nucleus for a given composition, temperature, and density (for details about ionization calculations, see Magee et al. 1995, and references therein). However, the tables do not cover completely the energy-dependent opacities for relatively low energies, $E \sim 10^{-4}$–10^{-2} keV. We complete this region using the free–free opacity, which is dominant[2] in this range and is given, in

[1] http://aphysics2.lanl.gov/cgi-bin/opacrun/tops_txt.pl

[2] This may not be strictly true for a heavy-element composition, such as Fe atmospheres. However, we use the free–free opacity in an energy range with

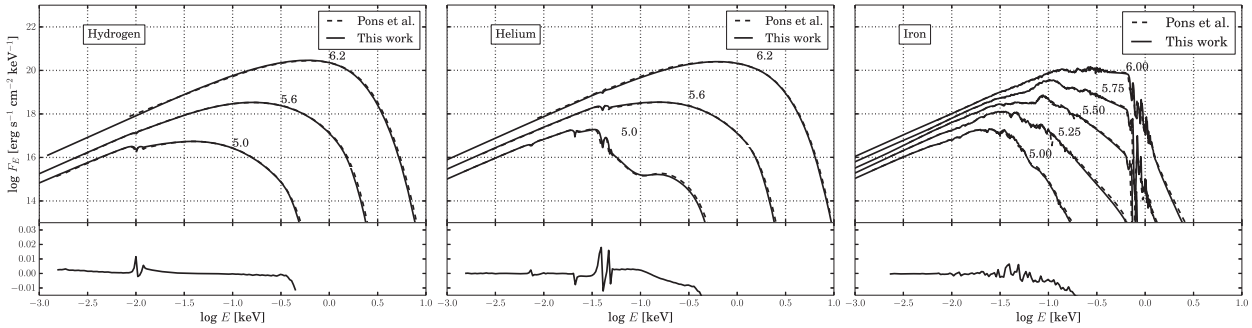

Figure 1. Spectra for non-magnetic NS atmospheres with pure H, He, and Fe compositions. All spectra are computed for an NS surface gravity $g_{\rm eff} = 2.43\times10^{14}\,{\rm cm\,s^{-2}}$. The logarithms of the effective NS surface temperatures are labelled in each spectrum. In all panels, the dashed lines correspond to the spectra computed by Pons et al. (2002), and the solid lines correspond to the spectra computed in this work. The lower panels show the fractional difference, $(f_0 - f_1)/f_0$, between the fluxes of this work, f_0, and those of Pons et al. (2002), f_1, for NS atmospheres with effective surface temperature $T_{\rm eff} = 10^{5.0}$ K.

CGS units, by Rybicki & Lightman (1979) as

$$\kappa_\nu^{\rm ff} = 3.7\times10^8\, T^{-1/2} n_{\rm e}^2 \sum_i n_i Z_i^2 \nu^{-3} \left(1 - {\rm e}^{-h\nu/kT}\right) \bar{g}_\nu^{\rm ff}(\nu, T), \quad (11)$$

where i labels the kind of ions, Z_i is the charge of the ions, n_i is the ion number density, and $\bar{g}_\nu^{\rm ff}$ is the Gaunt factor, also obtained from Rybicki & Lightman (1979).

2.3 Plasma effects

In the UV range, the emergent spectrum can be affected by absorption features due to atomic transitions in this energy range, as well as by plasma effects. The latter can be seen through the standard expression for the plasma frequency

$$\omega_{\rm p} = \left(\frac{4\pi e^2 n_{\rm e}}{m_{\rm e}}\right)^{1/2}, \quad (12)$$

where e is the electron charge, $n_{\rm e}$ is the electron number density, and $m_{\rm e}$ is the electron mass. This frequency can be estimated by combining the equation of hydrostatic equilibrium (equation 1) with an ideal gas EOS $P = nk_{\rm B}T$, where n is the particle density and $k_{\rm B}$ is the Boltzmann constant, yielding $n \sim g_{\rm eff}\tau/(\kappa_{\rm R} k_{\rm B} T)$. Assuming $n_{\rm e} \sim n$, an optical depth $\tau \sim 1$, a hydrogen Rosseland mean opacity $\kappa_{\rm R} \sim 10^4\,{\rm cm^2\,g^{-1}}$, and an effective surface gravity $g_{\rm eff} \sim 10^{14}\,{\rm cm\,s^{-2}}$, we obtain $\hbar\omega_{\rm p} \sim \hbar\left[4\pi e^2 g_{\rm eff}\tau/\left(m_{\rm e}\kappa_{\rm R} k_{\rm B} T\right)\right]^{1/2} \sim 1$ eV, which is close to the UV range and therefore may affect the analysis of *HST* observations of cool NSs.

In a plasma, the dispersion relation connecting the wavenumber, k, the frequency, ω, and the plasma frequency, $\omega_{\rm p}$, is given by

$$\omega = \left(\omega_{\rm p}^2 + c^2 k^2\right)^{1/2}, \quad (13)$$

where c is the speed of light. Since for $\omega < \omega_{\rm p}$ the wavenumber becomes imaginary, $\omega_{\rm p}$ defines a cut-off frequency below which there is no electromagnetic wave propagation in the plasma. Aharony & Opher (1979) showed that, for $\omega > \omega_{\rm p}$, the frequency-dependent opacities κ_ω should be replaced by

$$\kappa_\omega \rightarrow \frac{\kappa_\omega}{1 - (\omega_{\rm p}/\omega)^2}. \quad (14)$$

a relatively low radiative flux, where the atmosphere is optically thick, and the photosphere has a relatively small temperature gradient. This means that the emergent spectrum is largely unchanged by increasing the opacities, for example, due to additional bound–bound or bound–free transitions.

In other words, the frequency-dependent opacities tend to infinity when a photon with frequency just above $\omega_{\rm p}$ passes through the plasma. Thus, this correction to the frequency-dependent opacity has the effect, in the radiative transfer equation, of blocking the flux of photons with $\omega < \omega_{\rm p}$ through the plasma. We therefore incorporate these considerations into our NS atmosphere model calculation and quantify their effects, before applying these models to the UV/X-ray data of J0437.

3 MODEL COMPARISON AND RESULTS

In order to test our atmosphere calculation code, we generate spectra for different temperatures and compositions and compare them with the spectra of Pons et al. (2002) for H and He atmospheres with temperatures ranging from $T_{\rm eff} = 10^{5.0}$ to $10^{6.2}$ K, and for Fe atmospheres with effective temperatures ranging from $10^{5.0}$ to $10^{6.0}$ K. Like this work, Pons et al. (2002) follow a standard technique to model the NS atmosphere (Romani 1987; Rajagopal & Romani 1996) and compute the emergent spectrum using the LANL opacities. The main differences are that their calculations consider only 200 energy bins, compared to 900 in our case, and cover the range of Rosseland optical depths $10^{-8} < \tau_{\rm R} < 10^2$, whereas we used $10^{-3} < \tau_{\rm R} < 10^2$ for the comparison and $10^{-3} < \tau_{\rm R} < 10^3$ for all other calculations. The range $10^{-8} < \tau_{\rm R} < 10^{-3}$, which we do not cover, does not make a significant difference because very few photons are emitted or absorbed in this region. Including the interval $10^2 < \tau_{\rm R} < 10^3$, on the other hand, slightly increases the flux in the high-energy tail (worsening the agreement with Pons et al. 2002, as expected), but does not noticeably affect most of the spectrum.

Fig. 1 shows that the emergent spectra for H, He, and Fe compositions calculated with both codes do not show substantial differences. In particular, for $T_{\rm eff}^\infty = 10^{5.0}$ K, the fractional difference in the UV range, $-2.0 \lesssim \log(E/{\rm keV}) \lesssim -1.3$, is always < 2 per cent. The largest differences likely originate in the width of the energy bins (wider in the work of Pons et al. 2002), which do not fully resolve the absorption lines. The agreement is much better in regions away from these lines. We also compare our Fe spectra with those of Rajagopal & Romani (1996) finding no significant differences.

We compute spectra for pure H, He, and Fe atmospheres with and without plasma effects. The plasma frequency is obtained from the number of free electrons per nucleus, which is tabulated in the LANL opacity tables for a given composition, temperature, and density. Fig. 2 shows that the energy associated with the plasma

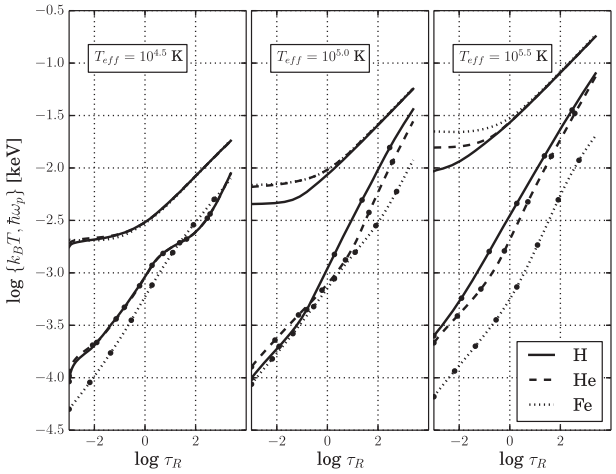

Figure 2. Thermal energy, $k_B T$, and energy associated with the plasma frequency, $\hbar\omega_p$, through the atmosphere of an NS with effective surface temperatures $T_{\rm eff} = 10^{4.5}$, $10^{5.0}$, and $10^{5.5}$ K. All curves correspond to an NS with mass $M_{\rm NS} = 1.5\,{\rm M}_\odot$ and radius $R_\infty = 15$ km. The upper solid, dashed, and dotted lines are the temperature profiles for H, He, and Fe atmospheres, respectively. Correspondingly, the lower lines with big dots are the energy associated with the plasma frequency for each atmosphere composition.

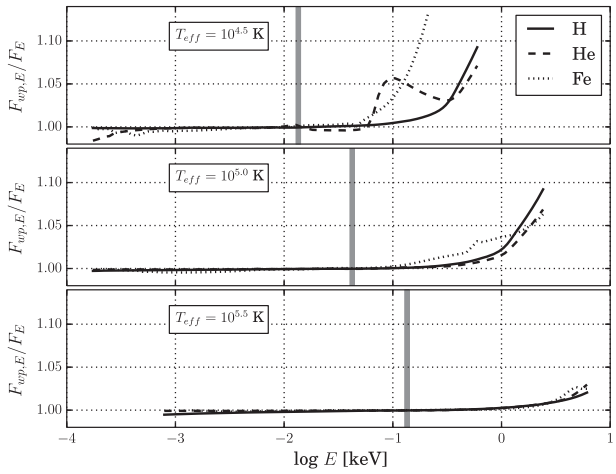

Figure 3. Ratio between fluxes for spectra with and without plasma frequency effects. The spectra are calculated considering $M_{\rm NS} = 1.5\,{\rm M}_\odot$, $R_\infty = 15$ km, and effective surface temperatures $T_{\rm eff} = 10^{4.5}$, $10^{5.0}$, and $10^{5.5}$ K. The solid, dashed, and dotted lines correspond to H, He, and Fe atmospheres, respectively. As a reference, the grey vertical lines indicate the energies where a BB with same $T_{\rm eff}$ has its maximal emission. The plasma frequency has the largest impact on the high-energy (Wien) tail of the spectrum of the coldest Fe atmosphere model, but far from the flux peak.

frequency, $\hbar\omega_{\rm p}$, is always substantially below the peak of the spectra $\sim k_{\rm B}T$. Since most of the flux is produced at energies $E \sim (1$–$10)k_{\rm B}T$, plasma effects block an insignificant part of the photon flux. This means that plasma frequency effects do not produce a significant change in the temperature profile and the structure of the atmosphere.

In addition, Fig. 3 shows that the plasma frequency effects change the spectra just slightly below $E \sim 10^{-3}$ keV and above $E \sim 10^{-1}$ keV for all effective surface temperatures considered. The flux below $E \sim 10^{-3}$ keV is reduced because low-energy photons are blocked at relatively low Rosseland optical depths. Instead, the flux increases above $E \sim 10^{-1}$ keV because, at high Rosseland optical depths, the plasma frequency blocks photons with higher energies, which, in order to conserve the radiative flux, requires a slight increase of the temperature in the inner parts of the atmosphere. In fact, since the opacities decrease at high energies, and the energy-dependent optical depth $\tau_E = 1$ is located at deeper zones, the emergent spectrum for $E \gtrsim 10^{-1}$ keV is sensitive to the plasma effects and to the change of the temperature profile in the inner parts of the atmosphere. However, even with this change in the atmosphere spectra, the overall effect in the relevant energy range $E \sim 10^{-2}$–1 keV of the thermal emission from J0437 (considering $T_{\rm eff} \sim 10^5$ K) is $\lesssim 2$ per cent for H/He composition and $\lesssim 4$ per cent for Fe composition.

For the analysis presented in this section, we have considered only three representative effective surface temperatures, $T_{\rm eff} = 10^{4.5}$, $10^{5.0}$, and $10^{5.5}$ K. Fig. 3 shows the tendency of plasma effects to become relatively less important, for all compositions, as the effective temperature of the atmosphere increases. Therefore, for $T_{\rm eff} > 10^{5.5}$ K, plasma effects should be negligible. On the other hand, for $T_{\rm eff} < 10^{4.5}$ K, the amount of free electrons throughout the atmosphere decreases for all compositions, i.e. the plasma becomes less ionized. However, at low temperatures (as shown in Fig. 3), plasma frequency effects may still produce a substantial change in the spectra of Fe atmospheres in the soft X-ray energy range, although relatively far from the flux peak (as a reference, see also Fig. 1). Thus, we conclude that plasma effects are not important in the thermal emission of MSPs (and any non-magnetic NSs) with light element atmosphere, but they may become important in very cold and heavy-element atmospheres, producing an enhancement of the soft X-ray emission,[3] but limited just to the high-energy (Wien) tail of the spectrum.

Fig. 4 shows the relation between the temperature inferred from a BB fit and that from an atmosphere model, considering the flux in the energy range $E^\infty = 6.2$–9.4 eV (as observed at infinity). In particular, for a fixed 'redshifted radius' or 'apparent radius' $R_\infty = (1+z)\,R_{\rm NS}$ and temperature $T \sim 10^5$ K, a BB fit roughly reflects the effective temperature for He and Fe atmospheres. Instead, a BB fit underestimates by a factor $\approx$2.1 the temperature with respect to a H atmosphere. In the range plotted, the temperature transformation between a BB and a H atmosphere can be fairly well described by the function $T_{\rm H}/T_{\rm BB} \equiv f_{\rm H} = -1.994x^3 + 29.42x^2 - 142.1x + 226.4$, where $x = \log(T_{\rm BB}[{\rm K}])$. Similarly, the temperature transformations from BB to He and Fe atmospheres can be described by the functions $f_{\rm He} = 1.674x^3 - 23.5x^2 + 110.4x - 172.6$ and $f_{\rm Fe} = -3.157x^3 + 48.65x^2 - 248.7x + 423.2$, respectively.

4 APPLICATIONS TO PSR J0437−4715

4.1 Fitting procedure, MCMC, and tests

We fit our spectral model of non-magnetic NS atmospheres to the UV and soft X-ray emission from J0437. For the UV band, we use spectroscopic and photometric data from *HST* observations by Kargaltsev et al. (2004) and Durant et al. (2012). For the soft

[3]In the case of a liquid/metallic phase, at the surface of a very cold NS, the plasma frequency can be very high and suppress the flux in a substantial portion of the energy range of the thermal radiation. However, the radiative transfer equations are no longer valid for this regime, and the study of this case is outside the scope of this paper.

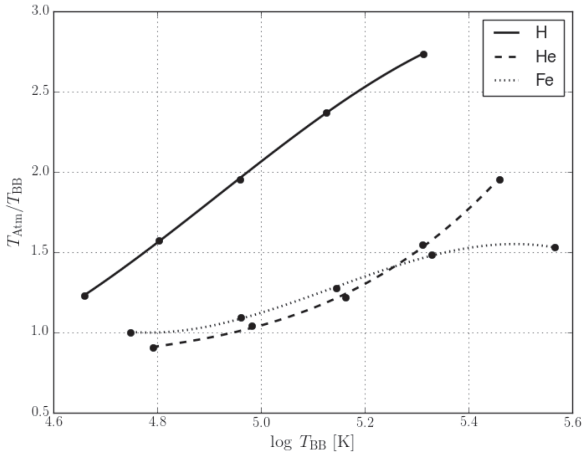

Figure 4. Temperature transformation between BB and atmosphere spectral fits for UV observations, considering the energy band $E^{\infty} = 6.2$–9.4 eV corresponding to the *HST* F140LP filter. The solid, dashed, and dotted lines show polynomial functions fitted for the temperature transformation (in black points) in the cases of H, He, and Fe atmosphere models, setting $M_{\rm NS} = 1.5\,{\rm M}_{\odot}$ and $R_{\infty} = 15$ km. For more details, see the last paragraph of Section 3.

X-ray band, we use *ROSAT* archive data (Becker & Trümper 1993) re-analysed by Guillot et al. (2016). We compute a χ^2 statistic between spectral models and UV/X-ray data considering four fitting parameters: interstellar extinction, $E(B-V)$, neutral hydrogen column density, $N_{\rm H}$, effective temperature, $T_{\rm eff}^{\infty}$, and radius, $R_{\rm NS}$, of the NS.

X-ray spectral fits account for the effects of interstellar neutral H via the absorption model of Wilms, Allen & McCray (2000). We fold the (absorbed) spectral model using the response matrix and effective area of the *ROSAT*-PSPC camera, taken from the HEASARC web page.[4] The folded X-ray spectra are binned in such a way that they match the energy binning of the *ROSAT* data presented in Guillot et al. (2016). CCD pile-up is not considered in our analysis as the X-ray data for J0437 show relatively low photon count rates. To compute the χ^2 statistic in the X-ray band, we considered only the $\sim$0.1–0.4 keV range, which is consistent with the cool thermal emission from the whole NS surface. In most of our analysis, we neglect the small contribution from the hot polar caps (Bogdanov 2013; Guillot et al. 2016), whose effect we evaluate approximately in Section 4.4.

We account for the dust effects in the UV fits using Milky Way extinction curves from Clayton et al. (2003), which are computed using the polynomial function from Fitzpatrick & Massa (1990), setting $R_V = 3.1$. Following Durant et al. (2012), we compute the χ^2 statistic in the UV band considering the 7–11 eV range of *HST* data, which is consistent with a Rayleigh–Jeans tail of the surface emission. As discussed in Durant et al. (2012), the spectrum of J0437 shows, just below $\sim$7 eV, a peaked optical/UV excess whose origin is still unknown (where the instrument spectral response is also rapidly decreasing).

To obtain the confidence levels for the fitted parameters, we run a set of Markov chain Monte Carlo (MCMC) simulations using the package `EMCEE` (Foreman-Mackey et al. 2013), considering four cases of emission models: H, He, and Fe atmosphere spectra and BB emission. The atmosphere spectra are obtained with log-scale

[4]https://heasarc.gsfc.nasa.gov/docs/rosat/pspc_matrices.html

Table 1. Spectral fit parameters with different models for J0437. The values of $R_{\rm NS}$, $T_{\rm eff}^{\infty}$, $N_{\rm H}$, and $E(B-V)$ are obtained from the MCMC posterior distributions. The values quoted are the medians (i.e. 50 per cent quantile), and the lower/upper uncertainties are obtained from the 16 and 84 per cent quantiles, so that they provide the 68 per cent credible intervals.

Model	$R_{\rm NS}$ (km)	$T_{\rm eff}^{\infty}$ (10^5 K)	$N_{\rm H}$ (10^{20} cm^{-2})	$E(B-V)$	χ^2/dof
H	$16.3^{+3.0}_{-2.5}$	$2.4^{+0.2}_{-0.2}$	1.7 ± 0.3	$0.06^{+0.03}_{-0.03}$	43.7/34
He	$15.1^{+2.7}_{-3.2}$	$2.5^{+0.2}_{-0.2}$	1.7 ± 0.3	$0.12^{+0.03}_{-0.04}$	45.3/34
Fe	$8.9^{+3.6}_{-2.4}$	$3.6^{+0.2}_{-0.2}$	2.3 ± 0.4	$0.15^{+0.06}_{-0.03}$	43.7/34
BB	$7.8^{+2.7}_{-1.9}$	$3.9^{+0.2}_{-0.2}$	2.8 ± 0.4	$0.15^{+0.03}_{-0.01}$	45.2/34
Gaussian prior on $E(B-V)$					
H	$13.1^{+0.9}_{-0.7}$	2.5 ± 0.1	1.6 ± 0.3	0.01 ± 0.01	45.2/34
Including hot polar caps and Gaussian prior on $E(B-V)$					
H	$13.6^{+0.9}_{-0.8}$	2.3 ± 0.1	1.4 ± 0.3	0.01 ± 0.01	45.9/34

polynomial interpolation from a 10×10 grid of models computed (from radiative transfer calculations; see Section 2) in a suitable range of temperatures and radii. We checked that the relative difference between interpolated spectra and actual atmosphere spectra is negligible, and we also found that our results remain largely unchanged by using, for example, a 5×5 temperature–radius grid. The models account for gravitational redshift considering an NS mass $M_{\rm NS} = 1.44\,{\rm M}_{\odot}$, and setting the source distance to $d = 156.79$ pc (Reardon et al. 2016).

We first considered uniform prior distributions in all the fitting parameters ($R_{\rm NS}$, $T_{\rm eff}^{\infty}$, $E(B-V)$, and $N_{\rm H}$), and then we refined our results with a Gaussian prior on $E(B-V)$, with boundaries for the MCMC equal to or larger than the limits shown in Figs 5(a)–(d). For each MCMC run, we used 100 walkers (chains) over 10 000 iterations. The first 25 per cent iterations of each run were excluded when generating the posterior distributions. We also checked convergence of the MCMC by visual inspection of the traces of parameters, and of the likelihood (χ^2), to ensure the proper mixing and sampling of the parameter space. The final minimum χ^2 values were statistically acceptable with values between 43.7 and 45.9 depending on the model, for 34 degrees of freedom.

4.2 Results of spectral fits with uniform priors

The results for the H, He, Fe, and BB spectral fits are summarized in Table 1. The spectral fits for all emission models have equally good χ^2 statistics. However, the results of our MCMC analyses, considering flat priors on all fitting parameters (Fig. 5), suggest that the H atmosphere model is favoured, as its posterior distributions for $E(B-V)$ and $N_{\rm H}$ show the best agreement with

(i) the measurements $E(B-V) < 0.012$ obtained with a 2D map[5] of infrared dust emission (Schlafly & Finkbeiner 2011, see also Schlegel, Finkbeiner & Davis 1998) and $E(B-V) = 0.002 \pm 0.014$ (for distances $d = 155$–160 pc to J0437) from a 3D map[6] constructed from starlight absorption by dust (see also Lallement et al. 2014; Capitanio et al. 2017; Lallement et al. 2018);

[5]https://irsa.ipac.caltech.edu/applications/DUST/
[6]https://stilism.obspm.fr

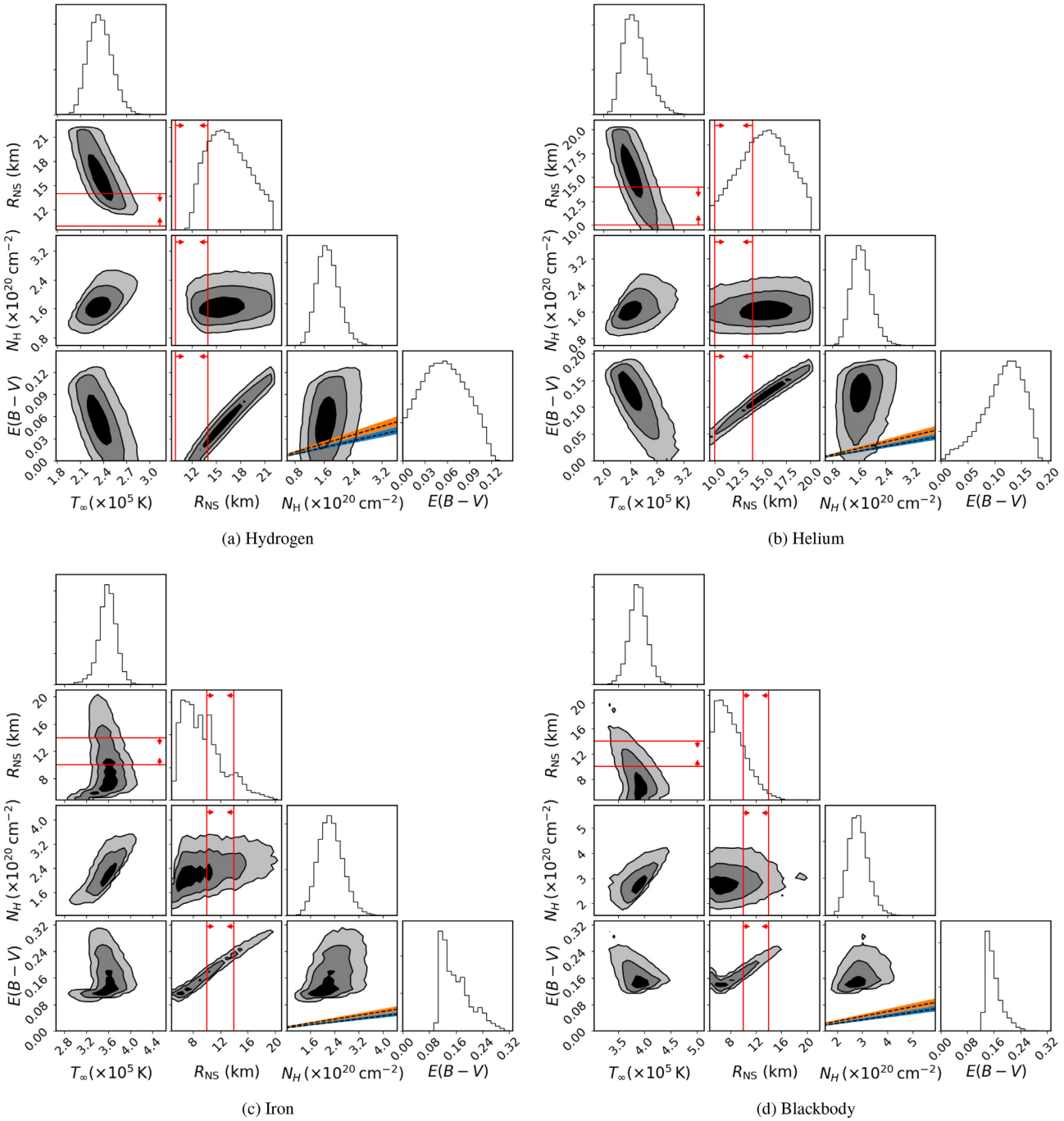

(a) Hydrogen (b) Helium

(c) Iron (d) Blackbody

Figure 5. MCMC marginalized (1D and 2D) posterior distributions for the fitting parameters used in the spectral analysis of J0437. The models are computed for non-magnetized, partially ionized NS atmospheres considering H, He, and Fe compositions, as well as BB emission (panels a–d). (For the H atmosphere model, the Lyman alpha absorption line was eliminated, as explained in Section 2.1.) The black, dark grey, and grey regions show the 68, 95, and 99.7 per cent confidence levels. The orange and blue bands show the $E(B-V)$–$N_{\rm H}$ relations (3σ enclosure around the central value as dashed lines) derived by Güver & Özel (2009) and Foight et al. (2016), respectively, for the Milky Way's interstellar medium. The red vertical lines with the arrows show the 99 per cent confidence range of the constraints on the NS radius obtained from the gravitational wave event GW 170817 (Abbott et al. 2018). While all compositions and the BB model produce sensible measurements of the NS properties, the H atmosphere model produces the best agreement with the empirical interstellar $E(B-V)$–$N_{\rm H}$ relations and $E(B-V)$ values from Galactic dust maps.

(ii) previous estimates of the interstellar dust extinction towards J0437 in the range $0.0 < E(B-V) < 0.07$ (Kargaltsev et al. 2004; Durant et al. 2012);

(iii) the correlation between $N_{\rm H}$ and A_V discussed by Foight et al. (2016) (see also Predehl & Schmitt 1995; Güver & Özel 2013): $N_{\rm H} = (2.81 \pm 0.12) \times 10^{21} A_V$, where $A_V = E(B-V) \times R_V$ and R_V is taken as 3.1.

Similar arguments suggest that the He atmosphere model is somewhat disfavoured, and the Fe atmosphere and BB models are ruled out.

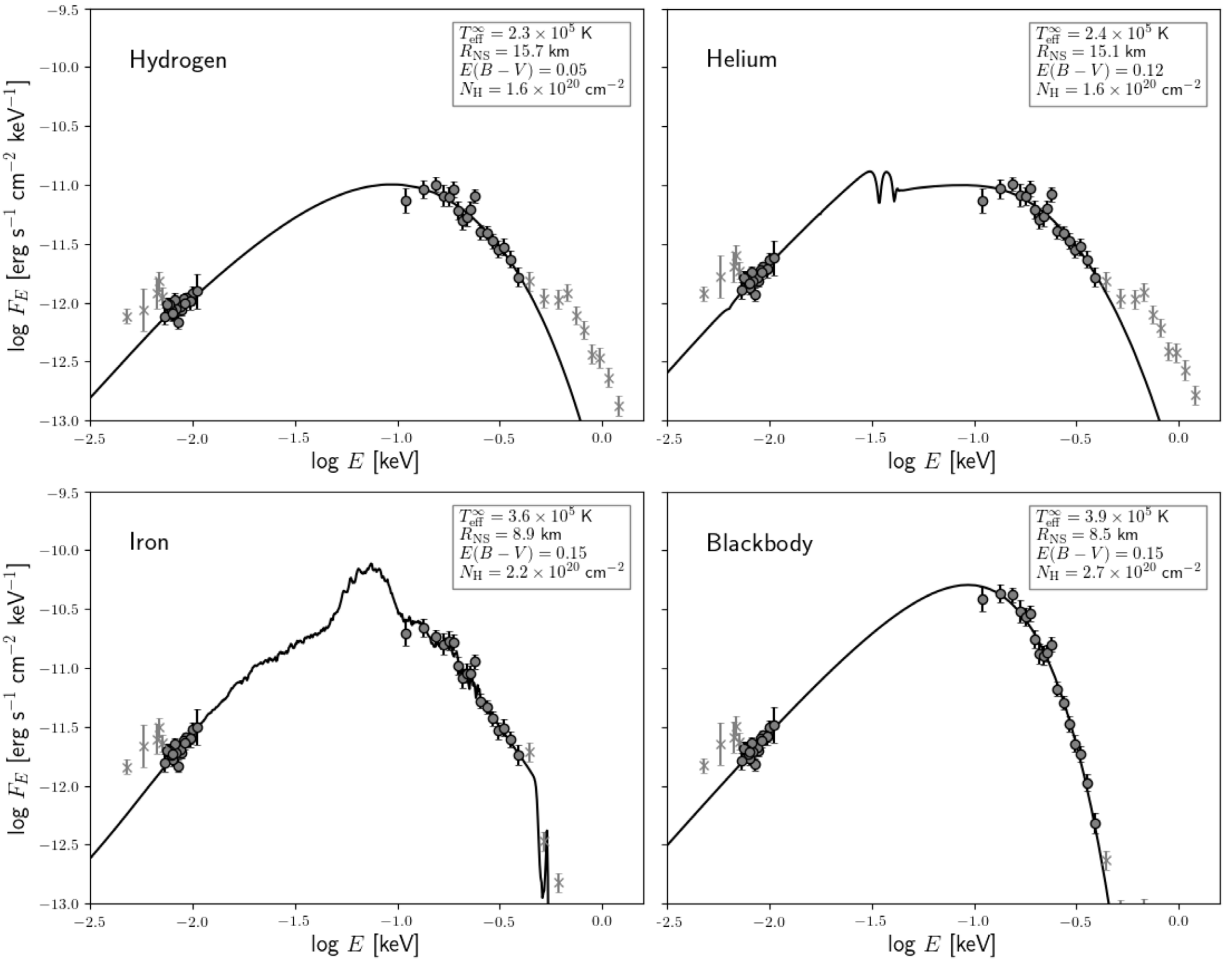

Figure 6. Best-fitting spectral models to the UV (*HST*) and soft X-ray (*ROSAT*) emission from J0437. In each panel, the solid lines show the spectral models computed for non-magnetized, partially ionized NS atmospheres considering H, He, and Fe compositions, as well as BB emission. The grey filled circles and cross symbols with error bars show the data used and not used in the spectral fits, respectively (for more details, see Section 4.1). The UV data correspond to dereddened fluxes, and the soft X-ray data correspond to unfolded, unabsorbed fluxes. Since the unfolding process depends on the assumed models, especially at the higher energies, and the best-fitting values for the extinction and hydrogen column density are also different, the plotted data points differ from one panel to another. The best-fitting values for $T_{\rm eff}^{\infty}$, $R_{\rm NS}$, $E(B-V)$, and $N_{\rm H}$ listed in each panel correspond to the peak of the posterior distribution shown in Fig. 5, whereas those listed in Table 1 are the posterior medians.

The posterior distributions for the H atmosphere model[7] produce a radius $R_{\rm NS} = 16.3^{+3.0}_{-2.5}$ km and a bulk surface temperature $T_{\rm eff}^{\infty} = (2.4 \pm 0.2) \times 10^5$ K, substantially cooler than the polar caps ($\gtrsim 10^6$ K). In particular, the radius measurement is consistent with the lower bound obtained from the analysis of the X-ray light curve (hot polar cap emission) of J0437 by Bogdanov (2013), or the analysis of the broad X-ray spectral shape (Guillot et al. 2016). Furthermore, the lower end of the posterior distribution for $R_{\rm NS}$ is also compatible with the 99 per cent confidence limits on the NS radius obtained from the gravitational wave signal detected from the NS–NS merger GW 170817 (Fig. 5a, red lines), determined assuming a parameterized EOS consistent with 1.97 $M_\odot$ (Abbott et al. 2018).

[7]Note that the constraints on the temperature and radius derived in our spectral fits are more restrictive than those reported by Durant et al. (2012), which were obtained with combined UV (*HST*) and soft X-ray data (*XMM–Newton*; spectral flux at $E = 600$ eV taken as an upper limit on the surface thermal emission), but considering a BB model and a range of NS radii between $R_{\rm NS} = 7$ km and $R_{\rm NS} = 24$ km.

The posterior distributions obtained with all atmosphere models show a strong correlation between $R_{\rm NS}$ and $E(B-V)$ and an anticorrelation between $T_{\rm eff}^{\infty}$ and $E(B-V)$. Therefore, an independent measurement of the dust extinction would strongly reduce the error intervals for the radius and temperature. If the extinction is negligible, as suggested by the Galactic dust maps mentioned above, the H atmosphere model can produce an NS radius as small as $R_{\rm NS} \sim 12$ km. A discussion of the MCMC analysis including a prior on $E(B-V)$ is given in Section 4.3.

Fig. 6 shows the best-fitting spectra obtained with the MCMC analysis for all emission models. The UV data are dereddened according to the best-fitting $E(B-V)$ and the soft X-ray data are unfolded[8] and transformed to unabsorbed flux using the best-fitting $N_{\rm H}$. Since the posterior distributions for $T_{\rm eff}$, $R_{\rm NS}$, $E(B-V)$, and $N_{\rm H}$ are non-Gaussian, the best-fitting parameters shown in Fig. 6 differ slightly from the posterior medians listed in Table 1.

[8]The soft X-ray data are unfolded as $X^{\rm data}_{\rm unfold} = X^{\rm data}_{\rm fold} \cdot S/S_{\rm folded}$, where $X^{\rm data}_{\rm fold}$ correspond to the folded data, S is the model spectrum, and $S_{\rm folded}$ is the spectral model folded according to the telescope response.

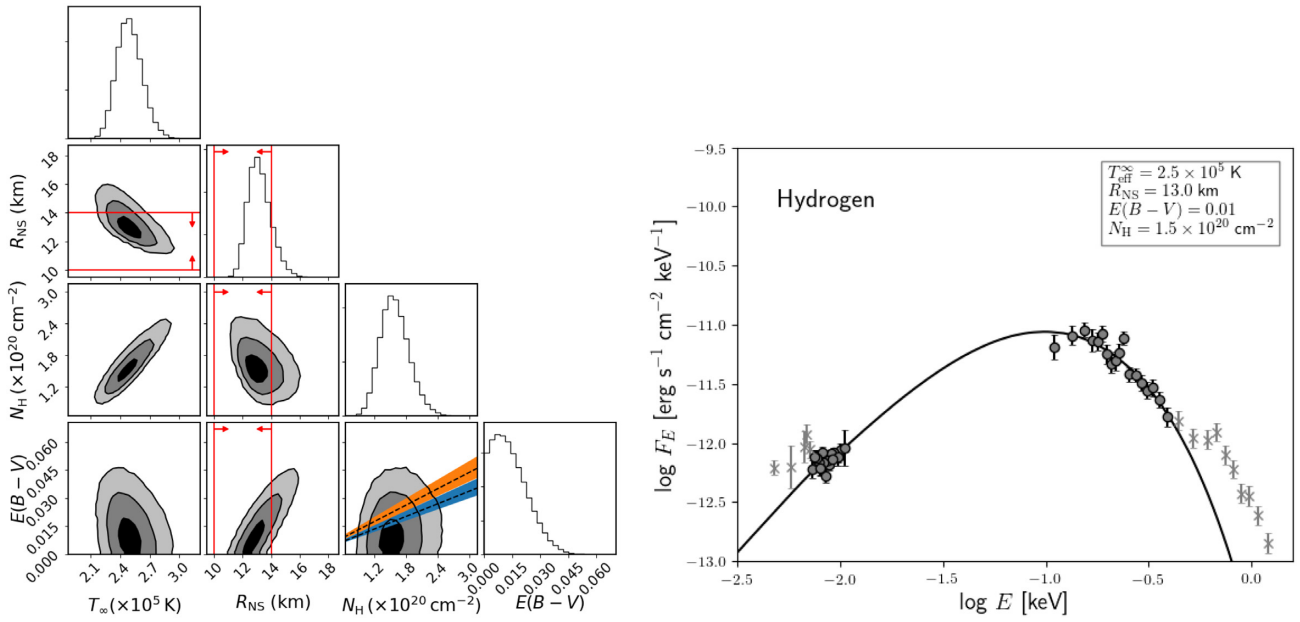

Figure 7. Same as Figs 5 and 6 for the H atmosphere model, but considering a Gaussian prior on $E(B-V)$.

4.3 NS radius estimation with a Gaussian prior on $E(B-V)$

J0437 is located in a region particularly devoid of dust.[9] As discussed in the previous section, 2D and 3D maps of dust extinction towards this source give $E(B-V) < 0.012$ and $E(B-V) = 0.002 \pm 0.014$, respectively. Furthermore, these values are compatible within 2σ with those derived with the MCMC analysis for the H atmosphere model (using flat priors in all the fitting parameters) and the empirical $N_{\rm H}$–$E(B-V)$ relation (Foight et al. 2016).

We repeat the MCMC analysis for the H atmosphere model including a Gaussian prior on $E(B-V)$, with mean $\mu_{\rm dust} = 0.002$ and standard deviation $\sigma_{\rm dust} = 0.014$, according to the latest 3D map of Galactic dust (Lallement et al. 2018), while ensuring $E(B-V) > 0$. A summary with the resulting medians for the fitting parameters is reported in Table 1. As expected, the results are compatible with those reported in Section 4.2. Remarkably, the uncertainties on the radius measurement are substantially reduced, yielding $R_{\rm NS} = 13.1^{+0.9}_{-0.7}$ km (see also the posterior distributions in Fig. 7).

4.4 Correction for hot polar caps and final radius estimate

Up to this point, we have neglected the effects on our fits from the hot polar caps, which are clearly identified in the X-ray data above $\sim$0.5 keV (Becker & Trümper 1993; Pavlov & Zavlin 1997; Bogdanov 2013; Guillot et al. 2016). In our low-energy spectral analysis, there could be two such effects:

(i) the low-energy tail of the hot components could directly contribute to the high end of the spectral range considered in our models;

(ii) the folded soft X-ray spectrum can be contaminated with high-energy photons due to the spectral response of the detector.

We tested the effect of the hot polar caps by adding two hot BB components to our H atmosphere fit (see Fig. 8). We used the parameters for the polar caps obtained by Guillot et al. (2016) for their H atmosphere + 2BB fit, which includes *NuSTAR*, *XMM–Newton*, and *ROSAT* data, covering the X-ray spectrum of J0437 up to 20 keV. Their best-fitting temperatures for the polar caps are $T^\infty_{\rm cap,1} = 1.8 \times 10^6$ K and $T^\infty_{\rm cap,2} = 3.4 \times 10^6$ K, with associated radii $R^\infty_{\rm cap,1} = 0.15$ km and $R^\infty_{\rm cap,2} = 0.03$ km, respectively. By including these fixed components in our MCMC analysis, we obtain a final NS radius estimation $R_{\rm NS} = 13.6^{+0.9}_{-0.8}$ km (a summary with all posterior medians is reported in Table 1). In comparison to the results reported in Section 4.3, the addition of the hot components makes the inferred bulk temperature decrease and the NS radius increase by amounts smaller than the estimated 1σ error bars.

A full analysis, including atmosphere model fits of the emission from both the hot polar caps and the cooler surface of the rest of the NS, is outside the scope of this paper and should be addressed using, for example, the hard X-ray data from *NuSTAR* and the high-quality soft X-ray data from the *NICER* mission. Furthermore, dealing with the hot polar cap emission requires to properly account for scattering opacity in the source function of our atmosphere models, which at the moment are suitable to model the cold thermal component of J0437 (see Section 2). Other uncertainties, such as the errors in the source distance or mass, are negligible in our analysis, as the errors are dominated by the much larger uncertainties, for example, in the interstellar extinction $E(B-V)$ (set as a fitting parameter in the MCMC analysis, with either a uniform or Gaussian prior).

5 DISCUSSION AND CONCLUSIONS

We modelled the cool thermal component of the spectrum of MSP J0437, observed in the UV (*HST*) and soft X-ray (*ROSAT*) bands, considering non-magnetized, partially ionized H, He, and Fe atmospheres. For surface temperatures $\sim 10^5$ K, as previously determined for this source (Kargaltsev et al. 2004; Durant et al. 2012), we found that plasma effects are negligible in the UV band (<1 per cent flux suppression), but may become important

[9] Lallement (private communication).

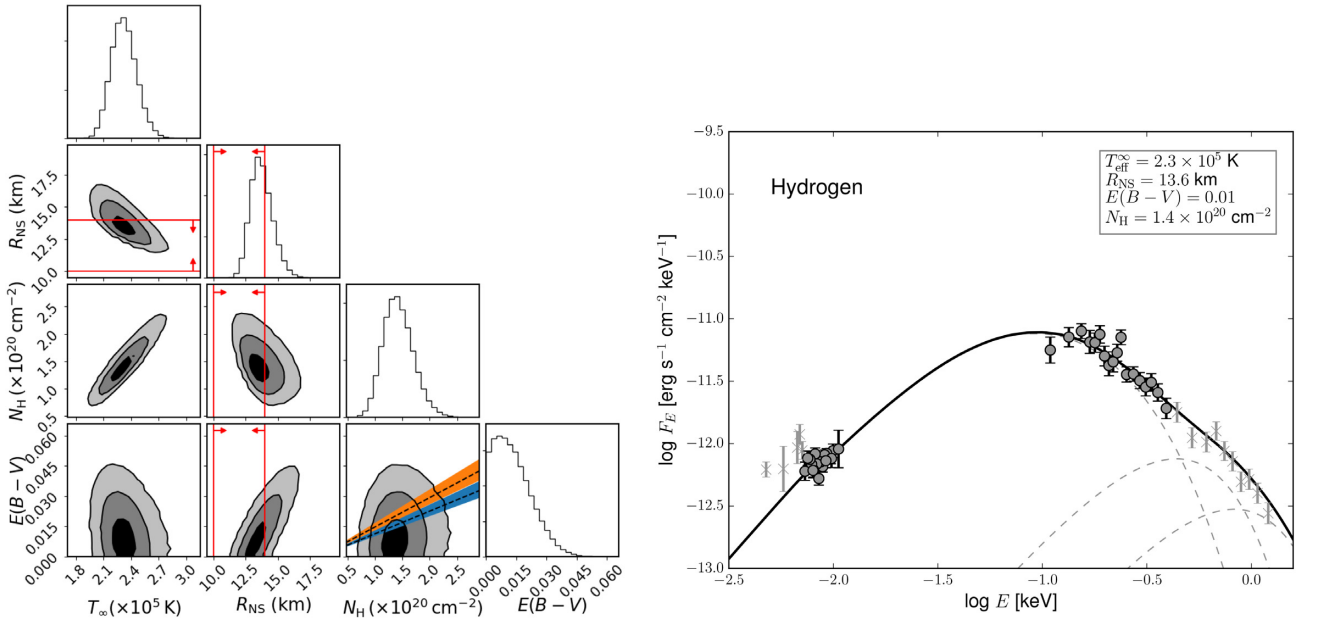

Figure 8. Same as Fig. 7, for the H atmosphere model, considering a Gaussian prior on $E(B-V)$, but accounting for the emission from the hot polar caps. In the right-hand panel, the black solid line corresponds to the H atmosphere model plus two hot BB models (for details, see Section 4.4). The grey dashed lines show the contribution of each component to the model spectrum. The UV and X-ray data (filled circles and crosses) are defined as in Fig. 6.

for cooler sources with heavy-element atmospheres, particularly for the emission in the soft X-ray band (in the Wien tail of the spectrum).

Using an MCMC analysis, we found that spectral fits to the UV/X-ray data of J0437 favour a H atmosphere composition, disfavour a He composition, and rule out Fe atmosphere composition as well as BB emission. This is consistent with the fact that BB emission cannot reproduce the observed pulsed amplitude of J0437 (Bogdanov 2013). For the H atmosphere composition, we found the following:

(i) By considering uniform priors in all fitting parameters, we obtain an NS radius $R_{NS} = 16.3^{+3.0}_{-2.5}$ km, a bulk surface temperature $T_{eff}^{\infty} = (2.4 \pm 0.2) \times 10^5$ K, a dust extinction value $E(B-V) = 0.06 \pm 0.03$, and a neutral H column density $N_H = (1.7 \pm 0.3) \times 10^{20}$ cm^{-2}.

(ii) By including a Gaussian prior on the dust extinction, based on current 3D maps of Galactic dust, we refine our measurements: $R_{NS} = 13.1^{+0.9}_{-0.7}$ km, $T_{eff}^{\infty} = (2.5 \pm 0.2) \times 10^5$ K, and $N_H = (1.6 \pm 0.3) \times 10^{20}$ cm^{-2}.

(iii) By accounting for the effect of the hot polar caps, we obtain our final results: $R_{NS} = 13.6^{+0.9}_{-0.8}$ km, $T_{eff}^{\infty} = (2.3 \pm 0.1) \times 10^5$ K, and $N_H = (1.4 \pm 0.3) \times 10^{20}$ cm^{-2}.

Our radius determination for J0437, combined with its well-measured mass, allows us to establish the tightest constraint on the EOS for ultradense matter to date (for a review, see Lattimer & Prakash 2016) from an MSP. As shown in Fig. 9, the constraint on M_{NS} (Reardon et al. 2016) and R_{NS} (this work) for J0437 combined with one of the largest measured masses for a pulsar (PSR J1614−2230; Demorest et al. 2010; Arzoumanian et al. 2018) favours a stiff EOS and disfavours a strange matter EOS. Precise 3D maps of Galactic dust, presently under development, based on *Gaia* data (see e.g. Lallement et al. 2019), and high-quality X-ray observation from the *NICER* mission, will further improve the radius estimation for J0437 and the constraints on the EOS.

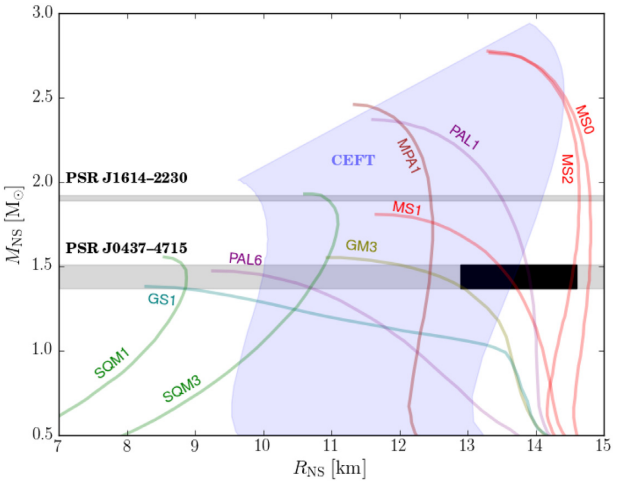

Figure 9. Mass–radius relation for different cold, superdense matter EOSs. The curves with different colours show a few EOSs, labelled as in Lattimer & Prakash (2001). The blue filled region labelled 'CEFT' shows a range of EOSs based on chiral effective field theory (Hebeler et al. 2013). The grey horizontal bands show the mass measurements for PSR J1614−2230 (Demorest et al. 2010; Arzoumanian et al. 2018) and J0437 (Reardon et al. 2016). The black region shows the radius measurement for J0437, at 1σ, obtained in this work.

Compared with other results, our measurement of R_{NS} for J0437 is

(i) consistent with the lower limits on the radius previously published for this source; specifically, Bogdanov (2013) derived $R_{NS} > 10.9$ km from the X-ray light curve (due to the hot polar caps), assuming a H atmosphere, while Guillot et al. (2016) obtained $R_{NS} > 10$ km from the soft X-ray spectrum (using a BB spectral component for the cool surface);

(ii) consistent with the constraints derived for two other MSPs: PSR J2124 and PSR J0030, with the associated lower limits $R_{\rm NS} > 7.8\,{\rm km}$ and $R_{\rm NS} > 10.4\,{\rm km}$, respectively (assuming $M_{\rm NS} = 1.4\,{\rm M}_{\odot}$; Bogdanov et al. 2008; Bogdanov & Grindlay 2009);

(iii) consistent with the NS radius derived from the NS–NS merger gravitational wave signal GW 170817 (Abbott et al. 2018);

(iv) consistent with the NS radius measurement from recent statistical analyses combining quiescent low-mass X-ray binaries (e.g. Steiner et al. 2018; Baillot d'Etivaux et al. 2019), which find radii in the 11–14 km range;

(v) slightly larger, but still marginally consistent with the NS radius obtained through the analysis of the cooling tails of X-ray bursts from the low-mass X-ray binary 4U 1702−429, $R_{\rm NS} = 12.4 \pm 0.4\,{\rm km}$ (Nättilä et al. 2017).

Our analysis also allowed us to test the surface composition of the MSP J0437. In particular, a H atmosphere is in agreement with the expectations for these sources, as such composition might result from (i) past accretion from a binary companion, (ii) accretion from the interstellar medium or (iii) spallation of heavier elements (Bildsten, Salpeter & Wasserman 1992). If other heavier elements coexist in the surface layers of NSs, they would stratify within ∼100 s (Romani 1987; Bildsten et al. 1992), leaving the lightest element on top. Furthermore, a very small amount of H, $\sim 10^{-20}\,{\rm M}_{\odot}$ (Bogdanov et al. 2016), is enough to produce an optical depth ∼1 in the X-rays (i.e. to form the atmosphere). On the other hand, the favoured H atmosphere composition of J0437 disfavours diffuse nuclear burning, or at least its effectiveness in modifying the atmosphere composition on $\sim 10^4$ yr time-scales (Chang & Bildsten 2003, 2004; Chang, Bildsten & Arras 2010) and produce external atmospheric layers with heavier elements. Systematic observations of the UV and soft X-ray emission from other MSPs may help us to establish further constraints on this issue.

The bulk surface temperature of J0437 derived in this work with the H atmosphere model is more restrictive than that obtained with a BB model by Durant et al. (2012) [$T_{\rm eff}^{\infty} = (1.5\text{–}3.5) \times 10^5\,{\rm K}$], which does not take into account the minimal value of $R_{\infty} = 3\sqrt{3}{\rm G}M/{\rm c}^2 = 11.0 \pm 0.5\,{\rm km}$ imposed by general relativity (considering the currently measured mass the pulsar $M_{\rm NS} = 1.44 \pm 0.07\,{\rm M}_{\odot}$; Reardon et al. 2016). Our temperature measurement is also relevant to understand the heating mechanisms that might be operating in NSs. Gonzalez & Reisenegger (2010) performed a comparative analysis of different heating mechanisms, finding that rotochemical heating (Reisenegger 1995, 1997; Fernández & Reisenegger 2005; Petrovich & Reisenegger 2010, 2011; González-Jiménez et al. 2015) and vortex creep (Alpar et al. 1984; Shibazaki & Lamb 1989; Larson & Link 1999) might explain the temperatures measured in old NSs. Rotation-induced crustal heating, which was proposed later (Gusakov, Kantor & Reisenegger 2015), could also be important. A full analysis of this issue will be presented in another work (Rodríguez et al., in preparation).

We note that our results rely on the assumption that non-magnetized atmosphere models appropriately describe the thermal emission from the entire surface of relatively cold NSs, such as J0437. The spin-down-derived magnetic field of this object, $B = 2.4 \times 10^8\,{\rm G}$, can affect the transport of radiation in the atmospheric plasma for electromagnetic waves with energies lower than the electron cyclotron energy $E_{\rm c}/(1+z) \sim 2\,{\rm eV}$, which is still below the UV band considered in our fits. Potentially, small-scale multipolar components present on the NS surface (stronger than the dipolar field) could affect the radiative transfer. If that is the case, and assuming that the transport of radiation becomes polarized (propagating in the so-called X and O modes), this would produce an excess in the optical/UV spectrum compared with the non-magnetized atmosphere model (see e.g. Ho & Lai 2001; Zane et al. 2001; Lloyd 2003; Suleimanov, Pavlov & Werner 2012). Such spectral fits will produce a smaller NS radius, so our results with non-magnetized atmosphere models may be considered as upper limits. A further caveat to consider is the possibility that no atmosphere is present on the cold surfaces of NSs (but probably at much lower surface temperatures than that of J0437), where the emission would arise directly from a liquid surface. However, no models exist so far to describe such emission from sources like MSPs.

ACKNOWLEDGEMENTS

We thank José Pons for providing us with NS spectra used to test these models and Rosine Lallement, George Pavlov, Andrew Cumming, Cristóbal Espinoza, Márcio Catelan, Thomas Tauris, Silvia Zane, Kinwah Wu, Mat Page, Ignacio Ferreras, Paul Kuin, Nicolás Viaux, and the ANSWERS group in Santiago for useful discussions that helped improve this paper. This research was supported by FONDECYT Regular Grant 1171421, ECOS-CONICYT Project C16U01, and CONICYT Basal Project AFB-170002. DG-C acknowledges the financial support of *Becas Chile* Fellowship No. 72150555. SG acknowledges the support of the French Centre National d'Études Spatiales (CNES).

REFERENCES

Abbott B. P. et al., 2018, Phys. Rev. Lett., 121, 161101
Aharony U., Opher R., 1979, A&A, 79, 27
Alpar M. A., Pines D., Anderson P. W., Shaham J., 1984, ApJ, 276, 325
Arzoumanian Z. et al., 2018, ApJS, 235, 37
Baillot d'Etivaux N., Guillot S., Margueron J., Webb N. A., Catelan M., Reisenegger A., 2019, preprint (arXiv:1905.01081)
Bailyn C. D., 1993, ApJ, 411, L83
Becker W., Trümper J., 1993, Nature, 365, 528
Bildsten L., Salpeter E. E., Wasserman I., 1992, ApJ, 384, 143
Bogdanov S., 2013, ApJ, 762, 96
Bogdanov S., Grindlay J. E., 2009, ApJ, 703, 1557
Bogdanov S., Grindlay J. E., Rybicki G. B., 2008, ApJ, 689, 407
Bogdanov S., Heinke C. O., Özel F., Güver T., 2016, ApJ, 831, 184
Capitanio L., Lallement R., Vergely J. L., Elyajouri M., Monreal-Ibero A., 2017, A&A, 606, A65
Chang P., Bildsten L., 2003, ApJ, 585, 464
Chang P., Bildsten L., 2004, ApJ, 605, 830
Chang P., Bildsten L., Arras P., 2010, ApJ, 723, 719
Clayton G. C., Wolff M. J., Sofia U. J., Gordon K. D., Misselt K. A., 2003, ApJ, 588, 871
Demorest P. B., Pennucci T., Ransom S. M., Roberts M. S. E., Hessels J. W. T., 2010, Nature, 467, 1081
Durant M., Kargaltsev O., Pavlov G. G., Kowalski P. M., Posselt B., van Kerkwijk M. H., Kaplan D. L., 2012, ApJ, 746, 6
Fernández R., Reisenegger A., 2005, ApJ, 625, 291
Fitzpatrick E. L., Massa D., 1990, ApJS, 72, 163
Foight D. R., Güver T., Özel F., Slane P. O., 2016, ApJ, 826, 66
Foreman-Mackey D., Hogg D. W., Lang D., Goodman J., 2013, PASP, 125, 306
Gänsicke B. T., Braje T. M., Romani R. W., 2002, A&A, 386, 1001
Gendreau K., Arzoumanian Z., 2017, Nat. Astron., 1, 895
Gendreau K. C. et al., 2016, in den Herder J.-W. A., Takahashi T., Bautz M., eds, Proc. SPIE Conf. Ser. Vol. 9905, Space Telescopes and Instrumentation 2016: Ultraviolet to Gamma Ray. SPIE, Bellingham, p. 99051H
Gonzalez D., Reisenegger A., 2010, A&A, 522, A16

González-Jiménez N., Petrovich C., Reisenegger A., 2015, MNRAS, 447, 2073
Guillot S. et al., 2016, MNRAS, 463, 2612
Guillot S., Pavlov G. G., Reyes C., Reisenegger A., Rodriguez L. E., Rangelov B., Kargaltsev O., 2019, ApJ, 874, 175
Gusakov M. E., Kantor E. M., Reisenegger A., 2015, MNRAS, 453, L36
Güver T., Özel F., 2009, MNRAS, 400, 2050
Güver T., Özel F., 2013, ApJ, 765, L1
Haakonsen C. B., Turner M. L., Tacik N. A., Rutledge R. E., 2012, ApJ, 749, 52
Hebeler K., Lattimer J. M., Pethick C. J., Schwenk A., 2013, ApJ, 773, 11
Heinke C. O., Wijnands R., Cohn H. N., Lugger P. M., Grindlay J. E., Pooley D., Lewin W. H. G., 2006, ApJ, 651, 1098
Ho W. C. G., Lai D., 2001, MNRAS, 327, 1081
Kargaltsev O., Pavlov G. G., Romani R. W., 2004, ApJ, 602, 327
Lallement R., Vergely J. L., Valette B., Puspitarini L., Eyer L., Casagrande L., 2014, A&A, 561, A91
Lallement R. et al., 2018, A&A, 616, A132
Lallement R., Babusiaux C., Vergely J. L., Katz D., Arenou F., Valette B., Hottier C., Capitanio L., 2019, A&A, 625, A135
Larson M. B., Link B., 1999, ApJ, 521, 271
Lattimer J. M., Prakash M., 2001, ApJ, 550, 426
Lattimer J. M., Prakash M., 2016, Phys. Rep., 621, 127
Lloyd D. A., 2003, PhD thesis, Harvard Univ.
Magee N. H. et al., 1995, in Adelman S. J., Wiese W. L., eds, ASP Conf. Ser. Vol. 78, Astrophysical Applications of Powerful New Databases. Astron. Soc. Pac., San Francisco, p. 51
Mihalas D., 1978, Stellar Atmospheres, 2nd edn. Freeman & Co., San Francisco
Miller M. C., 2016, ApJ, 822, 27
Nättilä J., Miller M. C., Steiner A. W., Kajava J. J. E., Suleimanov V. F., Poutanen J., 2017, A&A, 608, A31
Özel F., 2013, Rep. Prog. Phys., 76, 016901
Özel F., Psaltis D., Güver T., Baym G., Heinke C., Guillot S., 2016, ApJ, 820, 28
Pavlov G. G., Zavlin V. E., 1997, ApJ, 490, L91
Pavlov G. G., Rangelov B., Kargaltsev O., Reisenegger A., Guillot S., Reyes C., 2017, ApJ, 850, 79
Petrovich C., Reisenegger A., 2010, A&A, 521, A77
Petrovich C., Reisenegger A., 2011, A&A, 528, A66
Pons J. A., Walter F. M., Lattimer J. M., Prakash M., Neuhäuser R., An P., 2002, ApJ, 564, 981
Potekhin A. Y., 2014, Phys.-Usp., 57, 735
Predehl P., Schmitt J. H. M. M., 1995, A&A, 500, 459
Rajagopal M., Romani R. W., 1996, ApJ, 461, 327
Rangelov B., Pavlov G. G., Kargaltsev O., Reisenegger A., Guillot S., van Kerkwijk M. H., Reyes C., 2017, ApJ, 835, 264
Reardon D. J. et al., 2016, MNRAS, 455, 1751
Reisenegger A., 1995, ApJ, 442, 749
Reisenegger A., 1997, ApJ, 485, 313
Romani R. W., 1987, ApJ, 313, 718
Rybicki G. B., Lightman A. P., 1979, Radiative Processes in Astrophysics. Wiley, New York
Schlafly E. F., Finkbeiner D. P., 2011, ApJ, 737, 103
Schlegel D. J., Finkbeiner D. P., Davis M., 1998, ApJ, 500, 525
Shibazaki N., Lamb F. K., 1989, ApJ, 346, 808
Steiner A. W., Heinke C. O., Bogdanov S., Li C. K., Ho W. C. G., Bahramian A., Han S., 2018, MNRAS, 476, 421
Suleimanov V., Werner K., 2007, A&A, 466, 661
Suleimanov V. F., Pavlov G. G., Werner K., 2012, ApJ, 751, 15
Wilms J., Allen A., McCray R., 2000, ApJ, 542, 914
Zane S., Turolla R., Stella L., Treves A., 2001, ApJ, 560, 384
Zavlin V. E., 2007, preprint (astro-ph/0702426)
Zavlin V. E., Pavlov G. G., 1998, A&A, 329, 583
Zavlin V. E., Pavlov G. G., Shibanov Y. A., 1996, A&A, 315, 141
Zavlin V. E., Pavlov G. G., Sanwal D., Manchester R. N., Trümper J., Halpern J. P., Becker W., 2002, ApJ, 569, 894

This paper has been typeset from a TEX/LATEX file prepared by the author.